Electronic Supplementary Information

Activation of H_2 using *ansa*-aminoboranes: solvent effects, dynamics, and spin hyperpolarization

Karolina Konsewicz,[†a] Gergely Laczkó,[†b,c] Imre Pápai[b] and Vladimir V. Zhivonitko*[a]

[a.] NMR Research Unit, Faculty of Science, University of Oulu, P.O. Box 3000, Oulu, 90014, Finland. E-mail: vladimir.zhivonitko@oulu.fi.

[b.] Research Centre for Natural Sciences, Hungarian Academy of Sciences, Magyar Tudósok Körútja 2, H-1117 Budapest, Hungary.

[c.] Hevesy György Ph.D. School of Chemistry, Eötvös Loránd University, P.O. Box 32, H-1518 Budapest, Hungary.

-CONTENTS-

-LIST OF FIGURES-

-LIST OF TABLES-

1 Materials and experimental methods

1.1 General information

NMR experiments with parahydrogen were performed on a 400 MHz Bruker AV 400 NMR spectrometer equipped with a broad-band 5 mm RF probe. The standard temperature control unit of the NMR spectrometer was used for cooling and heating the samples. The kinetic (k_{as}, k_{dis}) and thermodynamic (K_c) parameter measurements were performed on a 600 MHz Spectrometer Bruker AV 600 NMR equipped with a broad-band 5 mm RF probe.

The studied ^{15}N-labelled *ansa*-aminoboranes **MesCAT-**^{15}N, **iPrPhCAT-**^{15}N and **PhCAT-**^{15}N referred in the text without "^{15}N" ending were synthesized using the procedures described in Ref.[S1]

High-purity H_2 gas was used for producing parahydrogen-enriched H_2 referred to in the main text as simply parahydrogen. The enrichment was performed with a Bruker parahydrogen generator, which produced H_2 gas with 92 % of parahydrogen.

1.2 PHIP NMR

1.2.1 Parahydrogen experiments

In a typical workflow, parahydrogen was bubbled trough a 0.05 M solution of the ansa-aminoboranes in degassed solvents (toluene-d8, acetonitrile-d3, dichloromethane-d2) in a 5 mm sample inside the NMR magnet for ca. 10 s, and then the parahydrogen flow was abruptly switched off and an NMR experiment was started. The bubbling procedure was performed under elevated pressure (5 bar) in the same manner as explained in detail in Ref.[S2] Parahydrogen was supplied to the bottom of the sample tube through a thin 360 μm fused silica capillary. The sample temperature was varied in the experiments when it was required. The sample preparation procedures were done under inert Ar atmosphere. The enhancement factors were determined by comparing the integral amplitudes of individual components of the enhanced ^{1}H NMR antiphase doublets to those in the thermal spectrum.

1.2.2 Theoretical aspects of revealing the longitudinal two spin order by application of a radio-frequency pulse

As a matter of fact, the accumulated non-equilibrium nuclear spin order in AAB-H_2 adduct, $\langle\hat{\rho}_e\rangle_b$, can be read out only indirectly after applying a radiofrequency pulse, because $\hat{\rho}_e$ itself is unobservable in NMR experiments. A hard π/4-pulse maximizes the NMR signal amplitudes of AX spin system sites in the ^{1}H NMR spectra, since antiphase transverse magnetization ($\hat{I}_{1x}\hat{I}_{2z} + \hat{I}_{1z}\hat{I}_{2x}$) is generated from $\hat{\rho}_e$ after the RF excitation:[S3]

$$\langle\hat{\rho}_{\mathrm{e}}\rangle_{\mathrm{b}}\hat{\rho}_{\mathrm{e}} \xrightarrow{\frac{\pi_y}{4}} \langle\hat{\rho}_{\mathrm{e}}\rangle_{\mathrm{b}}\left(\frac{\hat{E}}{4} - \frac{1}{2}\hat{I}_{1x}\hat{I}_{2z} - \frac{1}{2}\hat{I}_{1z}\hat{I}_{2x} - \frac{1}{2}\hat{I}_{1z}\hat{I}_{2z}\right). \quad (4)$$

The antiphase magnetization terms lead to observation of antiphase signals of NH and BH groups in the ^{1}H NMR and provide the strongest observed hyperpolarization effects in the experiments with *ansa*-aminoboranes represented in Figure 1 in the main text. This happens naturally due to the evolution under the isotropic Hamiltonian for *J*-coupled AX spin system with a significant resonance frequency separation as compared to the *J*-coupling constant value.[S3] Specifically, in the weak coupling regime, the anti-phase transverse magnetization evolves into the detected magnetization ($\hat{I}_{1y}$ and $\hat{I}_{2y}$) due to the scalar term in the Hamiltonian[S4]

$$\hat{I}_{1x}\hat{I}_{2z} + \hat{I}_{1z}\hat{I}_{2x} \xrightarrow{2\pi Jt\hat{I}_{1z}\hat{I}_{2z}} \cos(\pi Jt)\,\hat{I}_{1x}\hat{I}_{2z} + \frac{\sin(\pi Jt)}{2}\hat{I}_{1y} + \cos(\pi Jt)\,\hat{I}_{1z}\hat{I}_{2x} + \frac{\sin(\pi Jt)}{2}\hat{I}_{2y}, \quad (5)$$

giving rise to two enhanced anti-phase doublets corresponding to the NH and BH group signals in ^{1}H NMR spectra. The presence of coupling to heteronuclei (^{15}N and ^{11}B) leads to a replication of the antiphase doublets but generally does not change the hyperpolarization effect. Those couplings can be suppressed by application broad-band decoupling pulse sequences, similarly as it was used for ^{11}B in our experiments (Figure 5 in the main text).

1.2.3 Modelling of accumulation of the longitudinal two spin order

The full solution of the system of differential equations describing dynamics of accumulation and the decay of the longitudinal two spin order (Eqn. 3 and 4 in the main text) does not have a simple and compact form. However, one can elucidate main features coming from these equations by looking at the stationary state as described in the main text (Eqn. 5 and 6 in the main text).

The time evolution after parahydrogen bubbling was stopped is a bit easier to analyze since the source term ($k_0\langle\hat{\rho}_{\mathrm{e}}\rangle_0$) disappears and the underlying equations are converted into a homogeneous first order differential system. Therefore, we can analyze the decay of the longitudinal two spin order by finding eigenvalues of the following kinetic matrix

$$\mathbf{K} = \begin{pmatrix} -k_{\mathrm{as}}[\mathrm{AAB}]_0 - \frac{1}{T_{1\mathrm{f}}} & k_{\mathrm{dis}} \\ k_{\mathrm{as}}[\mathrm{AAB}]_0 & -k_{\mathrm{dis}} - \frac{1}{T_{1\mathrm{b}}} \end{pmatrix}. \quad (S1)$$

Assuming that the relaxation time of the longitudinal two spin order in the H_2 molecules (T_{1f}) is very long, one can neglect $\frac{1}{T_{1f}}$ term and find the following compact form of the eigenvalues

$$v_{\pm} = -\frac{S}{2}\left(1 \pm \sqrt{1 - \frac{4\,\theta\,\xi}{(1+\theta+\xi)^2}}\right), \quad (S2)$$

where

$$S = k_{\mathrm{as}}[\mathrm{AAB}]_0 + k_{\mathrm{dis}} + \frac{1}{T_{1b}} = k_{\mathrm{dis}}(1 + \xi + \theta), \quad \text{(S3)}$$

$$\xi = \frac{k_{\mathrm{as}}[\mathrm{AAB}]_0}{k_{\mathrm{dis}}} = \frac{[\mathrm{AAB{-}H_2}]_0}{[\mathrm{H_2}]_0}, \quad \text{(S4)}$$

$$\theta = \frac{1}{k_{\mathrm{dis}} T_{1\mathrm{b}}}. \quad \text{(S5)}$$

Note, that S constitutes the sum of kinetic and relaxation rates, while ξ and θ are concentration and relaxation factors, respectively.

Parameters $|v_{\pm}|$ represent fast and slow dynamics, respectively. As the first approximation, $|v_{+}|$ is not determining the rate of full decay of the spin order, but rather represents how fast the system will respond to the abrupt stop of parahydrogen bubbling. This can be elucidated from, e.g., comparison to the numerical solutions, or analytically. Therefore, we need to analyze $|v_{-}|$ to elucidate factors important for the relaxation of the spin order depicted on the second halves of Figures 5a and 5b of the main text.

As a matter of fact, to have a reasonable time for the detection of the hyperpolarized signals we need to have a sufficient time frame for stabilizing the sample after parahydrogen bubbling. In our experiments it was ca. 3 s. Therefore, it is desirable that the relaxation would not destroy the nuclear spin order significantly during this dead time. Moreover, it is generally important to have a long enough time frame to be able to use the hyperpolarization. To achieve this condition, $|v_{-}|$ must be minimized since this quantity represents the decay rate. Looking at Eq. S2, it is clear that requiring $\frac{4\,\theta\,\xi}{(1+\theta+\xi)^2}$ to be small will minimize $|v_{-}|$, while otherwise it will be large. The next level simplification can be derived if $\theta \ll 1$ or/and $\xi \ll 1$. In practice, it is equivalent to say that either relaxation or/and association kinetics are slow compared to the H_2 release kinetics. In this case, using series expansion ($\sqrt{1-x} \approx 1 - \frac{x}{2}$) one can find that

$$|v_{-}| \approx \frac{S\,\theta\,\xi}{(1+\theta+\xi)^2} = \frac{k_{\mathrm{dis}}\,\theta\,\xi}{1+\theta+\xi} = \frac{1}{T_{1b}} \cdot \frac{\xi}{1+\theta+\xi}, \quad \text{(S6)}$$

which represents the rate of the spin order decay ($\langle\hat{\rho}_{\mathrm{e}}\rangle_b \propto \exp(-|v_{-}|t)$), as was said above. This expression can be particularly important to estimate the efficiency of the chosen experimental protocol, given that kinetic and relaxation parameters are known. It can be simplified further if we assume that $\theta + \xi \ll 1$, i.e., that the relaxation is relatively slow compared to the dissociation reaction kinetics and H_2 pool is big compared to AAB-H_2 pool:

$$|v_{-}| \approx \frac{1}{T_{1\mathrm{b}}} \cdot \frac{[\mathrm{AAB{-}H_2}]_0}{[\mathrm{H_2}]_0}, \text{ when } \theta + \xi \ll 1. \quad \text{(S7)}$$

This is quite a common case when an elevated pressure of H_2 is used in the experiments and the catalyst is in a low concentration. The concentration dependence is explicitly visible in this case.

Therefore, both stationary amplitude of the spin order during the parahydrogen bubbling process as well as its decay after the bubbling show a clear concentration dependence through the concentration factor $\xi = \frac{[\mathrm{AAB{-}H_2}]_0}{[\mathrm{H_2}]_0}$.

This analysis immediately shows the drastic difference between **PhCAT** and **MesCAT** in toluene in terms of observed hyperpolarization effect. While relaxation times ($T_{1\mathrm{b}}$) are being on the same order of magnitude, the concentration factors, ξ, are dramatically different. The corresponding factors $\frac{\xi}{1+\theta+\xi}$ are ca. 0.4 and 0.005 for **PhCAT** and **MesCAT**, respectively. Almost a two orders of magnitude difference leads to a significantly faster decay of the nuclear spin order in the case of **PhCAT**, which prevents us from observation of any spin hyperpolarization effect after 3 s deadtime required for the sample stabilization (Figure 4e in the main text). The effective relaxation rate is ca. 0.6 s in this case as was estimated using kinetic and relaxation parameters for **PhCAT** at 298 K (see Table 1 of the main text). In contrast, around 2000-fold enhancement is observed for **MesCAT** under the same experimental conditions (Figure 4a in the main text), since the relaxation rate is more than one order of magnitude smaller (ca. 0.4/0.005 = 80 times slower decay rate).

This analysis also shows that changing the concentration factor, ξ, we can control the hyperpolarization amplitude. As defined by Eq. S4 and Eq. 7, this quantity can be decreased by decreasing the initial concentration of AABs. Indeed, dropping the concentration of **PhCAT** by 50 times led to the observation of hyperpolarization as shown in Figure 6 albeit at the price of the lowered thermal signals.

1.3 Results of kinetic measurements of H_2 activation

Herein, we present Eyring plots and typical examples of NMR spectra for the kinetic measurements. See the Experimental section in the main text for details of the kinetic measurement procedure.

1.3.1 Eyring plots used to determine enthalpies and entropies of activation

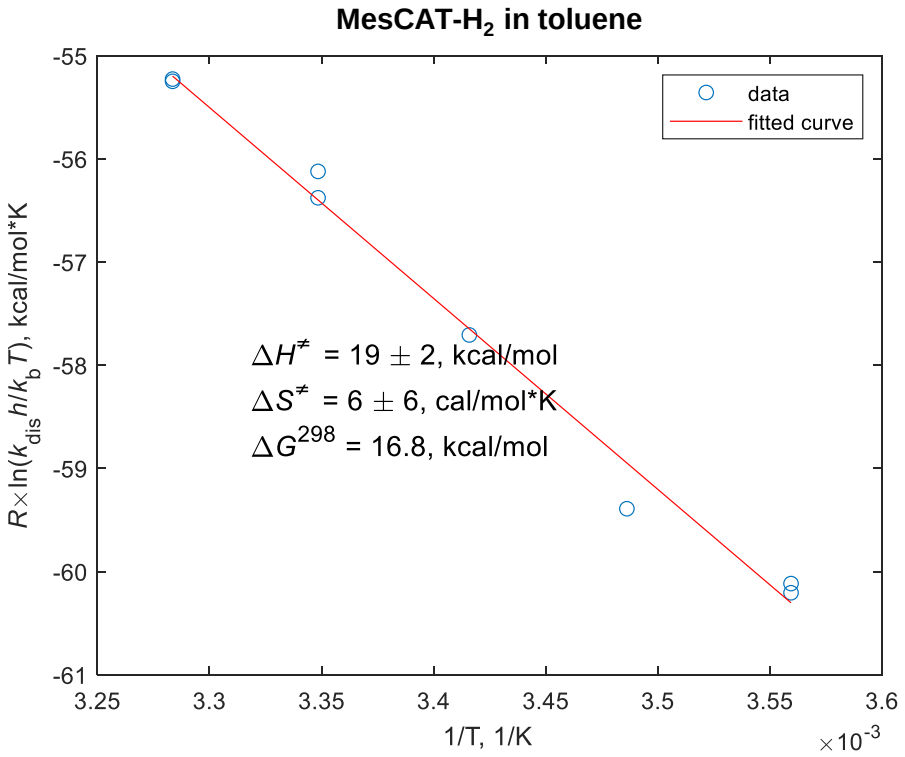

Figure S1. Eyring plot for **MesCAT-H₂** dissociation in toluene-d8. Experimental points are drawn with circles and the linear fitting result is shown with a red line. Experimentally measured rate constants and the activation parameters obtained from the fitting at 95% confidence level are also shown in the graph.

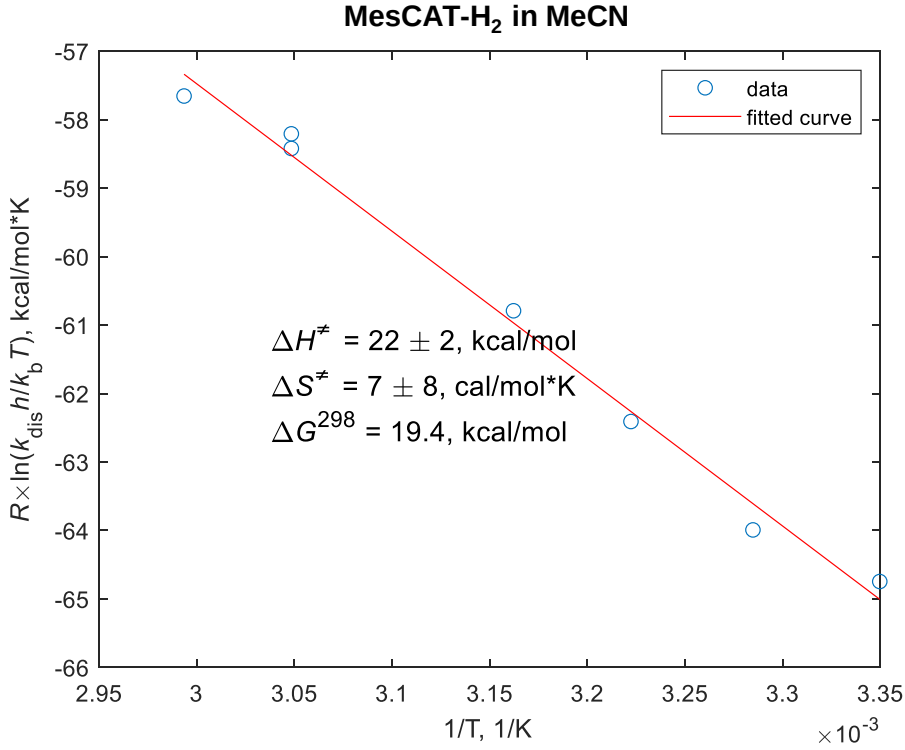

Figure S2. Eyring plot for **MesCAT-H₂** dissociation in acetonitrile-d3. Experimental points are drawn with circles and the linear fitting result is shown with a red line. Experimentally measured rate constants and the activation parameters obtained from the fitting at 95% confidence level are also shown in the graph.

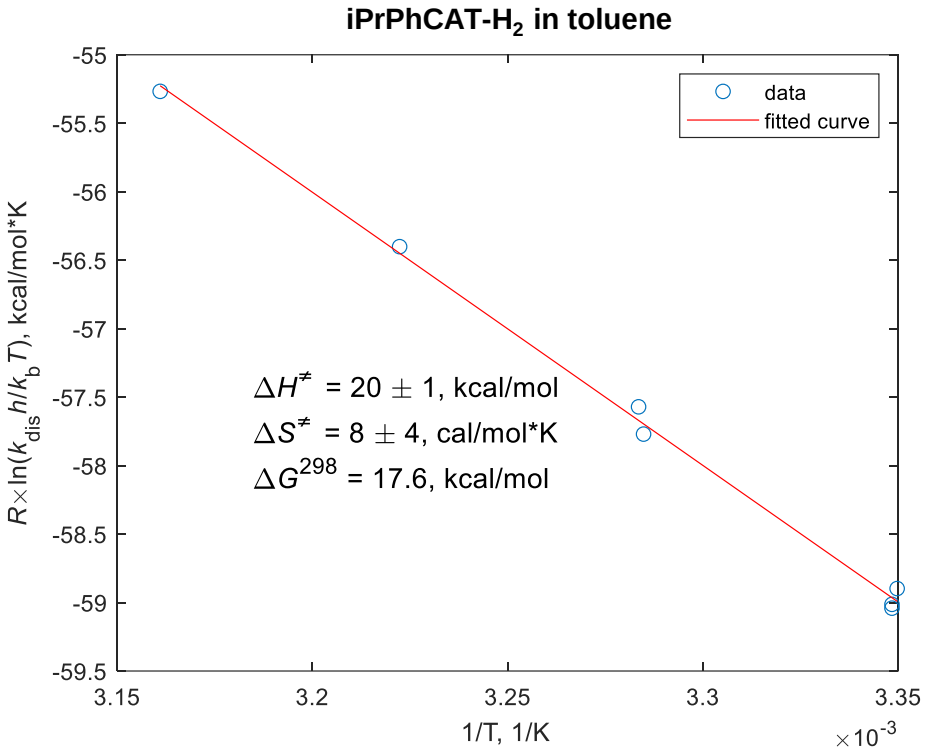

Figure S3. Eyring plot for **iPrPhCAT-H₂** dissociation in toluene-d8. Experimental points are drawn with circles and the linear fitting result is shown with a red line. Experimentally measured rate constants and the activation parameters obtained from the fitting at 95% confidence level are also shown in the graph.

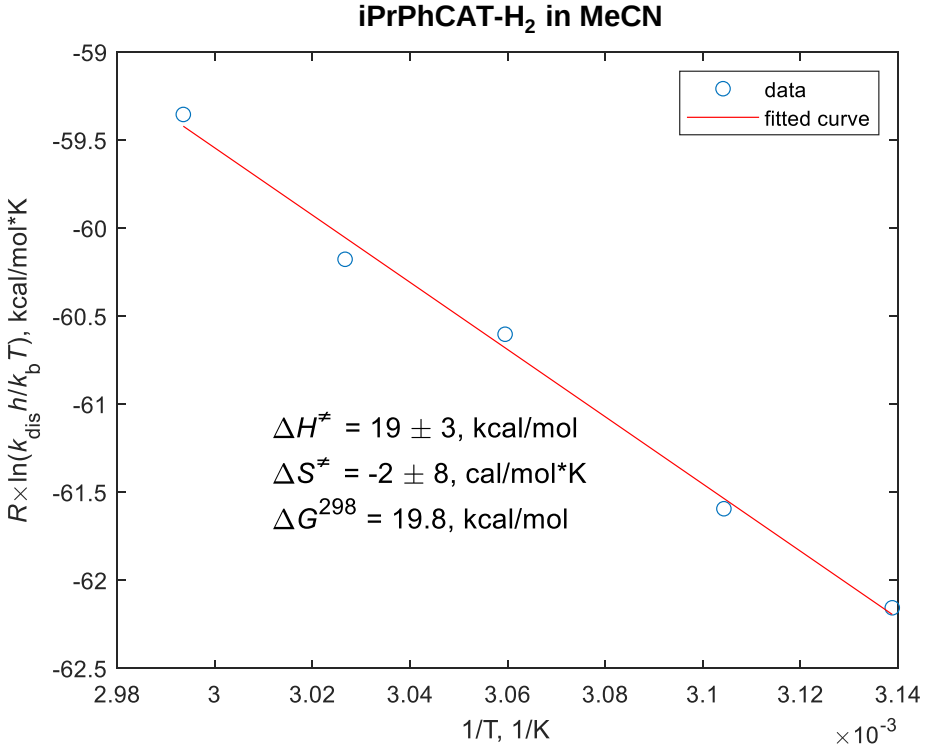

Figure S4. Eyring plot for **iPrPhCAT-H₂** dissociation in acetonitrile-d3. Experimental points are drawn with circles and the linear fitting result is shown with a red line. Experimentally measured rate constants and the activation parameters obtained from the fitting at 95% confidence level are also shown in the graph.

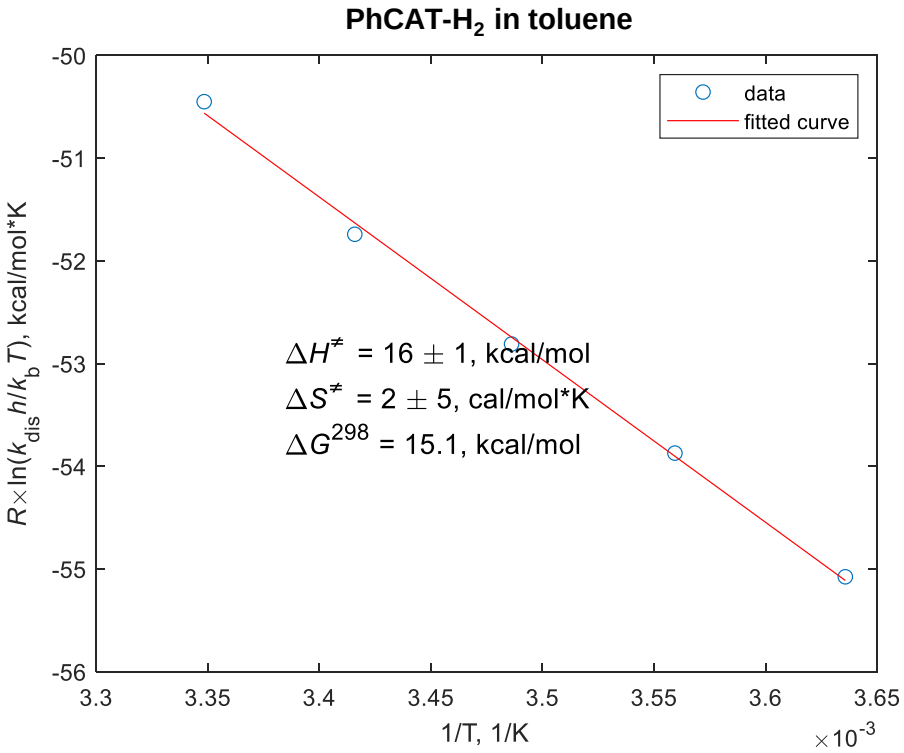

Figure S5. Eyring plot for **PhCAT-H₂** dissociation in toluene-d8. Experimental points are drawn with circles and the linear fitting result is shown with a red line. Experimentally measured rate constants and the activation parameters obtained from the fitting at 95% confidence level are also shown in the graph.

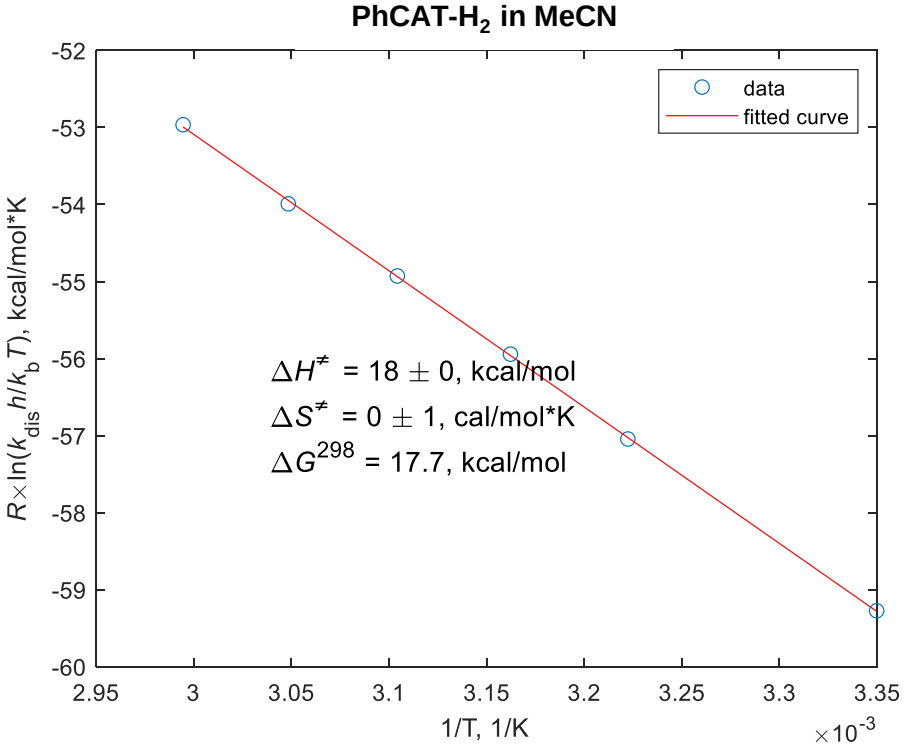

Figure S6. Eyring plot for **PhCAT-H₂** dissociation in acetonitrile-d3. Experimental points are drawn with circles and the linear fitting result is shown with a red line. Experimentally measured rate constants and the activation parameters obtained from the fitting at 95% confidence level are also shown in the graph.

1.3.2 Experimentally measured signal amplitudes used to determine K_c values

Equilibrium constants, $K_c = \frac{[AAB-H_2]_0}{[AAB]_0[H_2]_0}$, were determined via analysis of ^{1}H NMR spectra measured using various solvents in a selected range of temperatures. First, numerical integrals of the signals corresponding to *ansa*-aminoborane adducts (AAB-H_2), *ansa*-aminoboranes (AAB) and H_2 were calculated. In the case of AAB-H_2, NH group signals were used since they were well-separated from other peaks in a 9-12 ppm range depending on the solvent and temperature. Similarly, H_2 signal had non-overlapping resonance ca. 4.5-4.6 ppm and was easy to integrate. The determination of AAB integrals required more thorough analysis as some peaks were overlapping, but it was always possible to reliably integrate some of those peaks. The assignments of the signals used are presented in the spectra at the end of this section. Typically, a reference peak was also chosen in every spectrum to estimate detection sensitivity change as a function of temperature, but this effect was not very significant.

After the integrals were evaluated, their values normalized to the number of protons in the groups were used to compute $[AAB\text{-}H_2]_0/[AAB]_0$ (see tables below) ratios, whereas the hydrogen signal amplitude was converted into the molar concentration of H_2 species using known molar concentrations of AAB species. The reliability of this approach was confirmed by comparison to the known literature data on the solubility of H_2 in various solvents.[S5,6] Finally, the division of $[AAB\text{-}H_2]_0/[AAB]_0$ ratios by the determined molar concentrations $[H_2]_0$ gave the equilibrium constants K_c presented in Table 1 of the main text.

Furthermore, knowing K_c values as a function of temperature allowed us to extract standard enthalpies and entropies of the hydrogen activation using the standard equation

$$\ln\left(K_c(T)\right) = -\frac{\Delta G_r^0}{RT}, \quad \text{(S8)}$$

where

$$\Delta G_r^0 = \Delta H_r^0 - T\Delta S_r^0, \quad \text{(S9)}$$

through the linear least-square fitting of $\ln\left(K_c(T)\right)$ as a function of T^{-1}.

The corresponding association constant k_{ass} values were determined form K_c obtained as described above and k_{diss} obtained from the saturation transfer experiments, assuming that $K_c = k_{ass}/k_{diss}$, and therefore, $k_{ass} = K_c \times k_{diss}$.

1.3.2.1 MesCAT data

Table S1. Signal integrals and ratios extracted from ^{1}H NMR spectra for MesCAT in toluene.

Temperature, (K)	H_2 integral (A.U.)	$[AAB–H_2]_0/[AAB]_0$ ratio[a]	Average $[AAB–H_2]_0/[AAB]_0$ ratio[b]	H_2 conc. (M)	K_c (M^{-1})[a]	Average K_c (M^{-1})[b]
283	13.31	5.08E-03	5.07E-03	0.014	0.36	0.36
283	11.02	4.32E-03	4.35E-03	0.014	0.31	0.31
288	13.96	3.74E-03	3.72E-03	0.014	0.27	0.26
293	14.65	2.84E-03	2.83E-03	0.014	0.20	0.20
298	15.46	2.32E-03	2.34E-03	0.014	0.16	0.17
298	15.46	2.32E-03	2.34E-03	0.014	0.16	0.17
303	16.32	1.85E-03	1.80E-03	0.014	0.13	0.13
303	16.48	1.92E-03	1.80E-03	0.014	0.14	0.13

[a]Methyl group signal of **MesCAT** at 2.17 ppm was used.
[b]All identified peaks of **MesCAT** were used to calculate the average values.

Table S2. Signal integrals and ratios extracted from ^{1}H NMR spectra for **MesCAT** in acetonitrile.

Temperature, (K)	H_2 integral (A.U.)	$[AAB–H_2]_0/[AAB]_0$ ratio[a]	Average $[AAB–H_2]_0/[AAB]_0$ ratio[b]	H_2 conc. (M)	K_c (M^{-1})[a]	Average K_c (M^{-1})[b]
322.9	2.07	0.048	0.050	0.0195	2.45	2.57
312.9	1.97	0.077	0.083	0.0185	4.17	4.51
307.9	1.82	0.11	0.108	0.018	6.32	6.00
302.9	1.83	0.15	0.146	0.0175	8.37	8.33
297.9	1.88	0.20	0.198	0.017	11.68	11.66
322.9	2.07	0.043	0.044	0.0195	2.20	2.24
328	1.87	0.031	0.033	0.0205	1.54	1.59
298	1.72	0.22	0.215	0.017	13.04	12.66

[a]Aryl group signal of **MesCAT** at 7.15 ppm was used.
[b]All identified peaks of **MesCAT** were used to calculate the average values.

1.3.2.2 iPrPhCAT data

Table S3. Signal integrals and ratios extracted from ^{1}H NMR spectra for **iPrPhCAT** in toluene.

Temperature, (K)	H_2 integral (A.U.)	$[AAB–H_2]_0/[AAB]_0$ ratio[a]	Average $[AAB–H_2]_0/[AAB]_0$ ratio[b]	H_2 conc. (M)	K_c (M^{-1})[a]	Average K_c (M^{-1})[b]
303.0	16.35	0.295	0.311	0.015	19.69	20.71
298.0	12.73	0.362	0.384	0.0145	24.97	26.48
293.0	11.09	0.480	0.498	0.014	34.28	35.57
288.0	11.25	0.605	0.650	0.014	43.24	46.41
298.0	15.69	0.418	0.452	0.0145	28.82	31.16
302.9	16.04	0.317	0.329	0.015	21.12	21.91

307.9	17.67	0.229	0.246	0.0155	14.80	15.88
313.0	19.09	0.166	0.172	0.016	10.35	10.74
297.9	11.72	0.339	0.361	0.0145	23.39	24.88

[a]Methyl group signal of **iPrPhCAT** at 3.7 ppm was used.
[b]All identified peaks of **iPrPhCAT** were used to calculate the average values.

Table S4. Signal integrals and ratios extracted from ^{1}H NMR spectra for **iPrPhCAT** in acetonitrile.

Temperature, (K)	**H_2 integral (A.U.)**	**$[AAB–H_2]_0/[AAB]_0$ ratio[a]**	**H_2 conc. (M)**	**K_c (M^{-1})[a]**
328.00	75.73	4.76	0.020	230.52
324.90	69.79	5.56	0.0195	285.70
321.90	60.27	7.14	0.01985	368.59
317.90	73.59	10.00	0.01925	502.29
314.90	66.46	12.50	0.0189	643.02

[a]Methyl group signal of **iPrPhCAT** at 2.37 ppm was used.

1.3.2.3 PhCAT data

Table S5. Signal integrals and ratios extracted from ^{1}H NMR spectra for **PhCAT** in toluene.

Temperature (K)	**H_2 integral (A.U.)**	**$[AAB–H_2]_0/[AAB]_0$ ratio[a]**	**Average $[AAB–H_2]_0/[AAB]_0$ ratio[b]**	**H_2 conc. (M)**	**K_c (M^{-1})[a]**	**Average K_c (M^{-1})[b]**
293	1.70	0.328	0.322	0.014	23.43	22.97
298	1.78	0.261	0.262	0.014	18.65	18.67
288	1.54	0.415	0.361	0.014	29.57	31.45
283	1.26	0.546	0.505	0.014	38.91	36.04
278	0.89	0.685	0.649	0.014	48.76	46.31

[a]Aryl group signal of **PhCAT** at 7.01 ppm was used.
[b]All identified peaks of **PhCAT** were used to calculate the average values.

Table S6. Signal integrals and ratios extracted from ^{1}H NMR spectra for **PhCAT** in acetonitrile.

Temperature (K)	**Integral of H_2 (A.U.)**	**$[AAB–H_2]_0/[AAB]_0$ ratio[a]**	**H_2 conc. (M)**	**K_c (M^{-1})[a]**
297.90	17.75	14.29	0.017	858.05
307.90	18.45	7.69	0.018	415.93
312.90	18.64	5.26	0.0185	282.80
317.90	20.85	3.70	0.0190	192.30
322.96	19.79	3.45	0.0200	171.91
327.90	21.58	2.04	0.0205	98.48

[a]Methyl group signal of **PhCAT** at 1.62 ppm was used.

1.3.3 Signal assignments in NMR spectra for the kinetic measurements

1.3.3.1 MesCAT

Toluene: Selected ^{1}H NMR signals assigned to **MesCAT** and **MesCAT-H$_2$** are provided bellow (600 MHz, C_7D_8, δ, ppm):

MesCAT: 7.67 (d, 1 H, J = 7.28 Hz), 7.45 (d, 1H, J = 7.99 Hz), 6.76 (s, 4H), 2.20 (S, 6H), 2.17 (s, 12H), 1.16 (s, 6H), 0.99 (s, 6H), and 4.55 (s, H_2)

MesCAT-H$_2$: 8.57 (s, 1H, NH).

Reference peak (**R**): 0.32.

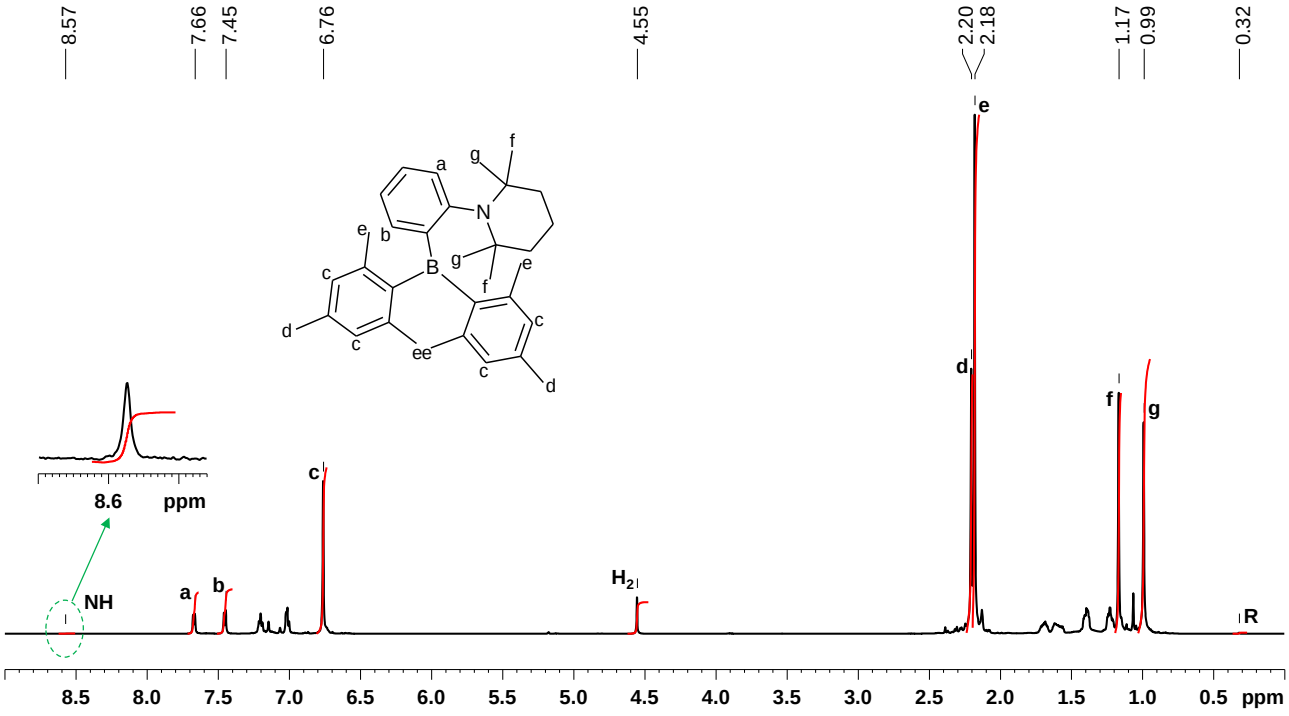

Figure S7. ^{1}H NMR Spectrum of a 0.05 M solution of MesCAT in toluene-d8.

Acetonitrile: Selected ^{1}H NMR signal assigned to **MesCAT** and **MesCAT-H$_2$** are provided bellow (600 MHz, CD_3CN, δ, ppm):

MesCAT: 7.54 (d, 1 H, J = 7.92 Hz), 7.42 (d, 1H, J = 7.92 Hz), 6.80 (s, 4H), 2.27 (S, 6H), 2.24. (s, 12H), f - 1.07 (s, 6H), g - 0.87 (s, 6H), and 4.60 (s, H2).

MesCAT-H$_2$: 8.64 (s, 1H, NH).

Reference peak (**R**): 7.15.

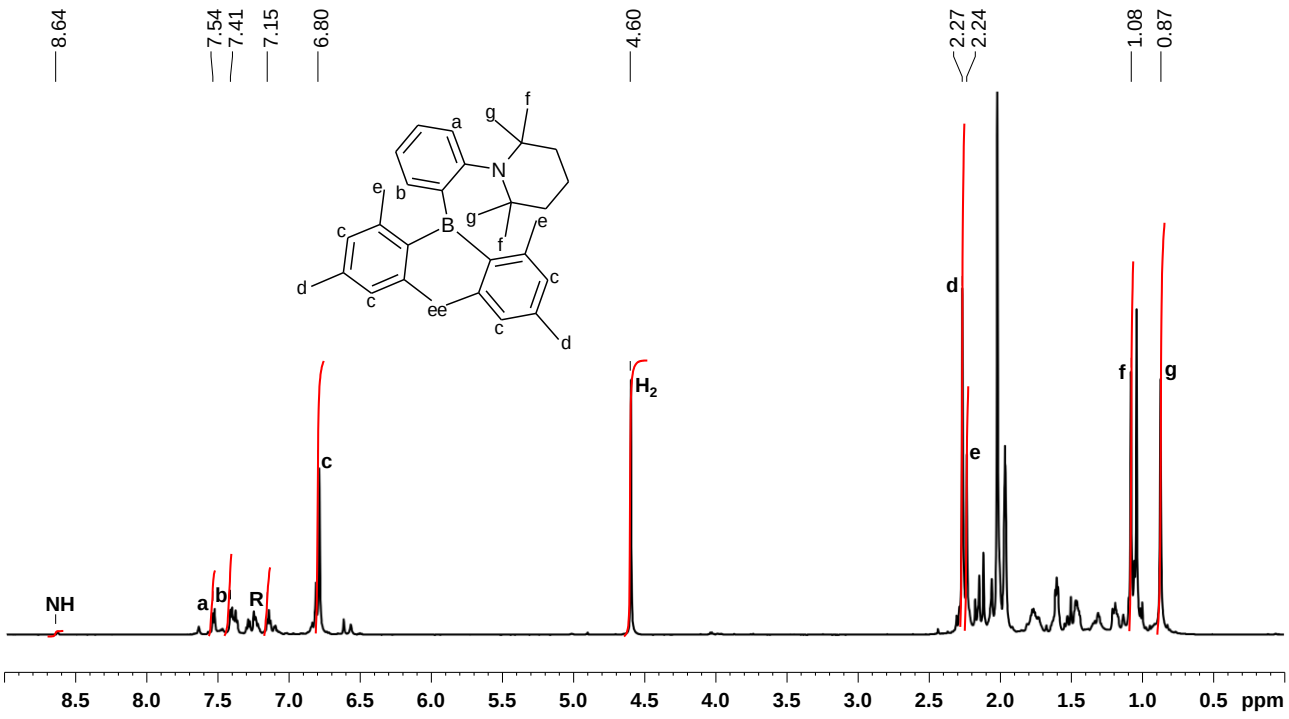

Figure S8. ^{1}H NMR Spectrum of a 0.05 M solution of **MesCAT** in acetonitrile-d3.

1.3.3.2 iPrPhCAT

Toluene: Selected ^{1}H NMR signal assigned to **iPrPhCAT** and **iPrPhCAT-H$_2$** are provided bellow (400 MHz, C_7D_8, δ, ppm):

iPrPhCAT: 7.51 (d, 2H J = 7.47 Hz), 7.48 (d, 2H, J = 7.89 Hz), 3.083 (m, 2H, J = 6.7 Hz), 1.056 (s, 12H), and 4.54 (s, H2).

iPrPhCAT-H$_2$: 9.66 (s, 1H, NH).

Reference peak (**R**): 3.22.

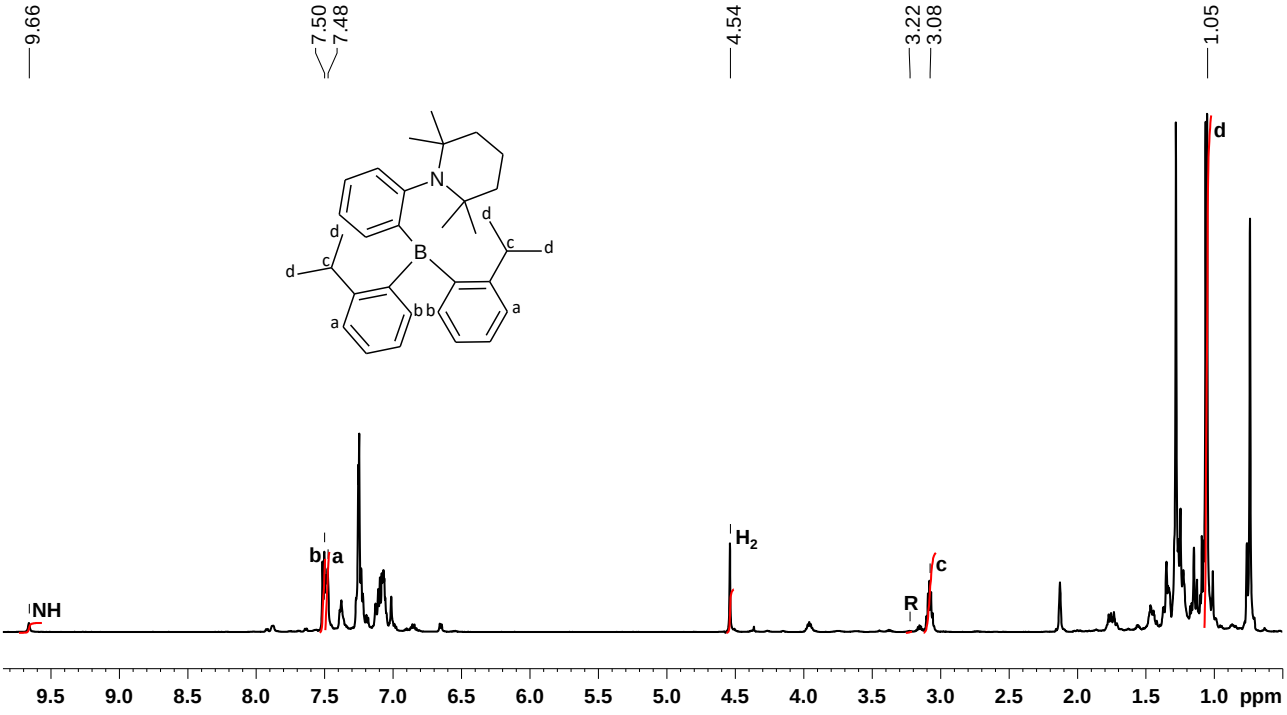

Figure S9. ^{1}H NMR Spectrum of a 0.05 M solution of **iPrPhCAT** in toluene-d8.

Acetonitrile: Selected ^{1}H NMR signal attributed to substrate and adduct are provided bellow (600 MHz, CD_3CN, δ, ppm):

iPrPhCAT: 0.67 (s, 6H), 2.94 (1 H) and 4.60 (s, H2).

iPrPhCAT-H$_2$: 9.41 (s, 1H, NH).

Reference peak (**R**): 2.37.

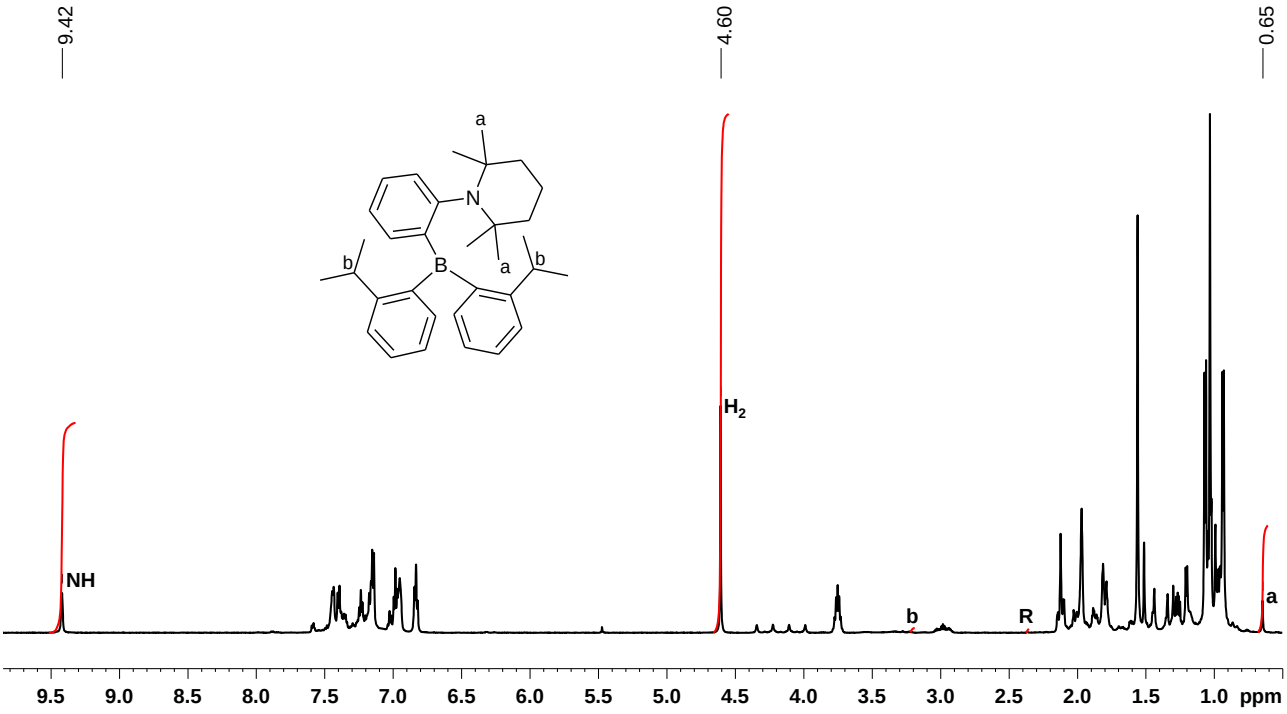

Figure S10. ^{1}H NMR Spectrum of a 0.05 M solution of **iPrPhCAT** in acetonitrile-d3.

Due to heavy overlapping of the adduct peaks with those of the substrate, assigning all peaks of **iPrPhCAT** was not possible. The complex nature of the overlapped peaks made it challenging to distinguish between the two **iPrPhCAT** and **iPrPhCAT-H$_2$**. For instance, there is an uncertainty in assignment of methyl groups in aromatics and TMP.

1.3.3.3 PhCAT

Toluene: Selected ^{1}H NMR signal attributed to substrate and product are provided bellow:

(400 MHz, C_7D_8, δ, ppm)

PhCAT: 7.64(d, 4H, J = 5.38 Hz), 7.48 (d, ^{1}H, J = 7,83 Hz), 7.24 (s, 6H), 1.25 (s, 6H), 0.69 (s, 6H), and 4.56 (s, H_2)

PhCAT-H_2: 10.86 (s, ^{1}H, NH)

Reference peak (**R**): 7.06.

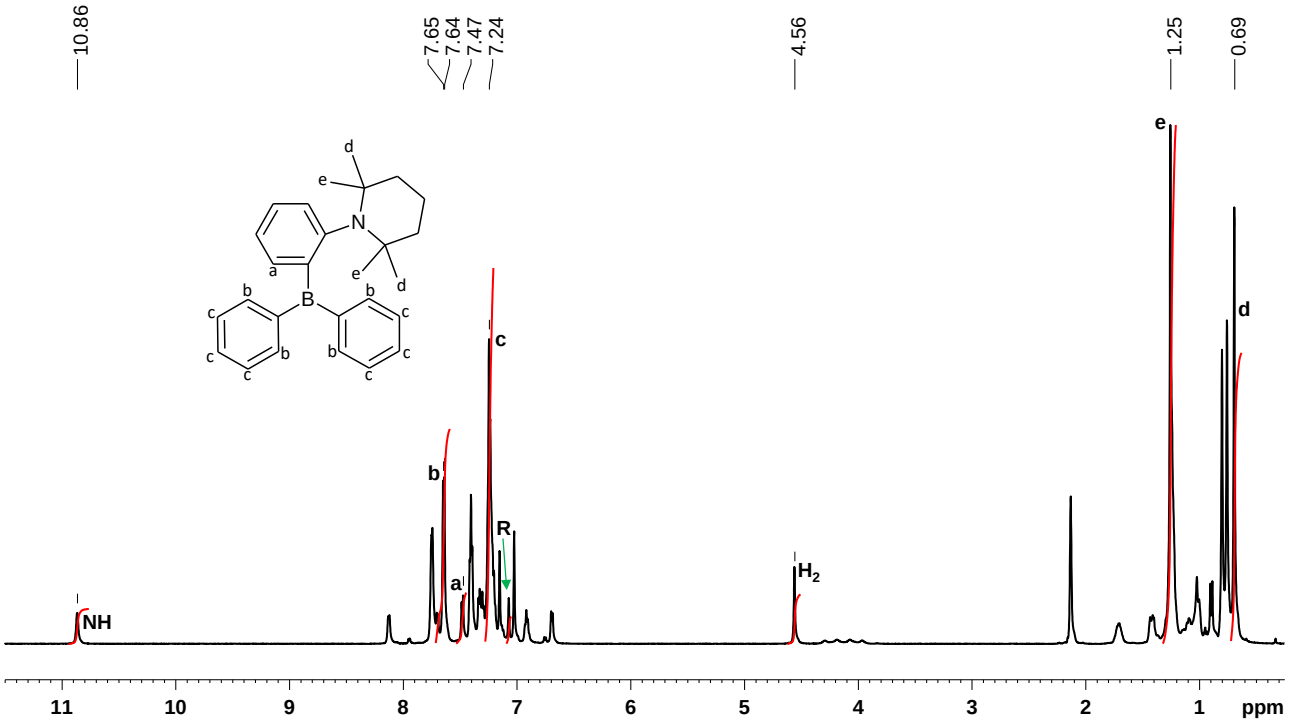

Figure S11. ^{1}H NMR Spectrum of a 0.05 M solution of **PhCAT** in toluene-d8.

Acetonitrile: Selected ^{1}H NMR signal attributed to substrate and adduct are provided bellow (600 MHz, CD_3CN, δ, ppm):

PhCAT: 0.57 (s, 6H), and 4.60 (s, H2)

PhCAT-H$_2$: 10.52 (s, 1H, NH).

Reference peak (**R**): 1.62.

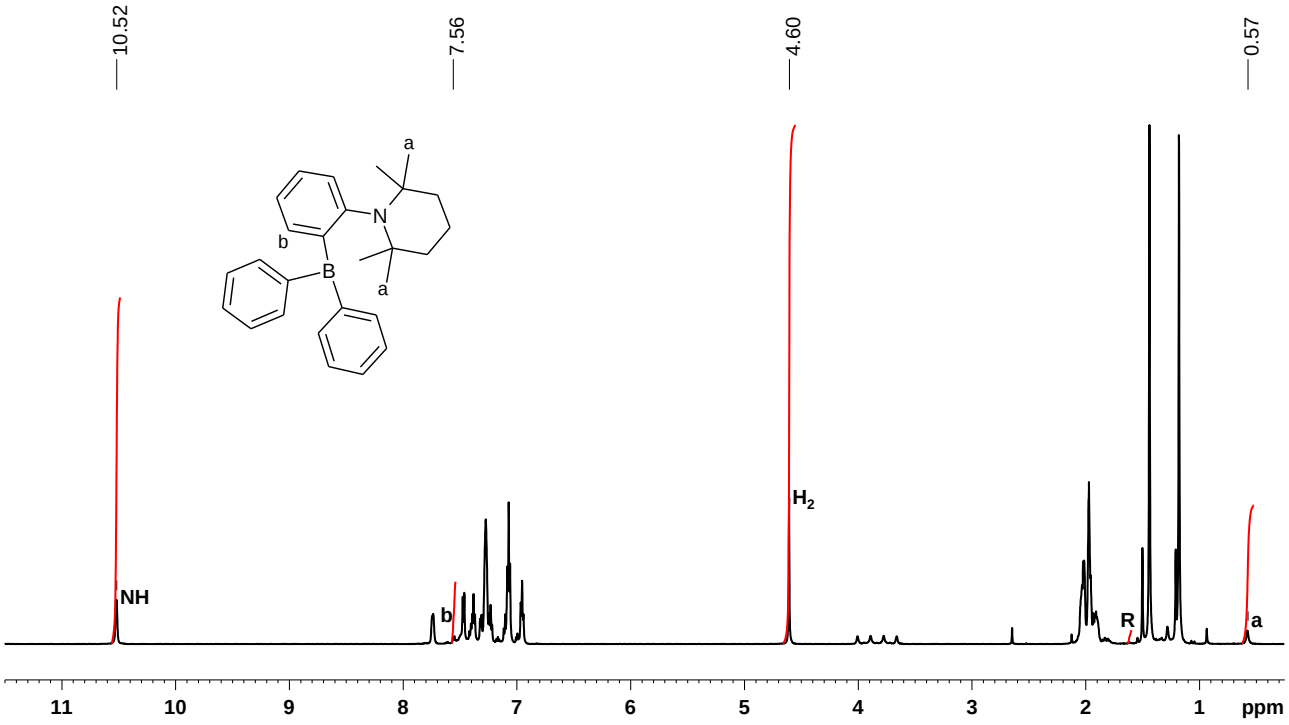

Figure S12. ^{1}H NMR Spectrum of a 0.05 M solution of **PhCAT** in acetonitrile-d3.

Due to heavy overlapping of the adduct peaks with those of the substrate, assigning additional peaks to the substrate was not possible. The complex nature of the overlapping peaks made it challenging to distinguish between **PhCAT** and **PhCAT-H$_2$**.

2 Computational details

All DFT calculations were carried out using *Gaussian16*.[S7] The ωB97X-D[S8] functional was chosen as this dispersion-corrected range-separated hybrid method was found to describe hydrogen activation via FLP accurately. All structures were optimized in the gas-phase at the ωB97X-D/6-311g(d,p) level. Thermal and entropic corrections were calculated at the same level of theory and within Grimme's quasi-RRHO approximation.[S9] The solvation Gibbs free energy was calculated also at the ωB97X-D/6-311g(d,p) level using the gas-phase structures and the SMD implicit solvation model.[S10] The electronic energies were recalculated at the ωB97X-D/6-311++G(3df,3pd) level of theory. The final Gibbs free energies were calculated according to the following formula:

$$G = E_0' + (G_0 - E_0) + (G_{sol} - E_0) + \Delta G_{conc},$$

where E_0 and E_0' refer to electronic energies computed at the ωB97X-D/6-311g(d,p) and the ωB97X-D/6-311++G(3df,3pd) levels of DFT, respectively; G_0 denotes the gas-phase Gibbs free energy; G_{sol} is the energy in solution-phase. ΔG_{conc} refers to the concentration correction (all Gibbs free energies were computed at the temperature 298.15 K and were corrected to the 1 mol/dm^3 concentration).

The conformational search was carried out for the more flexible *ansa*-aminboranes and their H_2-adduct with the MacroModel utility of the Scrödinger program[S11] and with the OPLS3e[S12] force field. The most promising structures were optimized with DFT and the most stable one was chosen accordingly.

2.1 Inversion of the TMP site: a- and b-forms of AAB and AAB-H₂

The conformations of the *ansa*-aminoboranes and their H_2 adducts can be categorized as **a** and **b** conformers according to the orientation of the TMP ring and these conformers may have different stabilities. The corresponding structures are depicted in Figure S13 and their relative stabilities in DCM are summarized in Table S7. The relative stabilities are almost identical when using the other solvents.

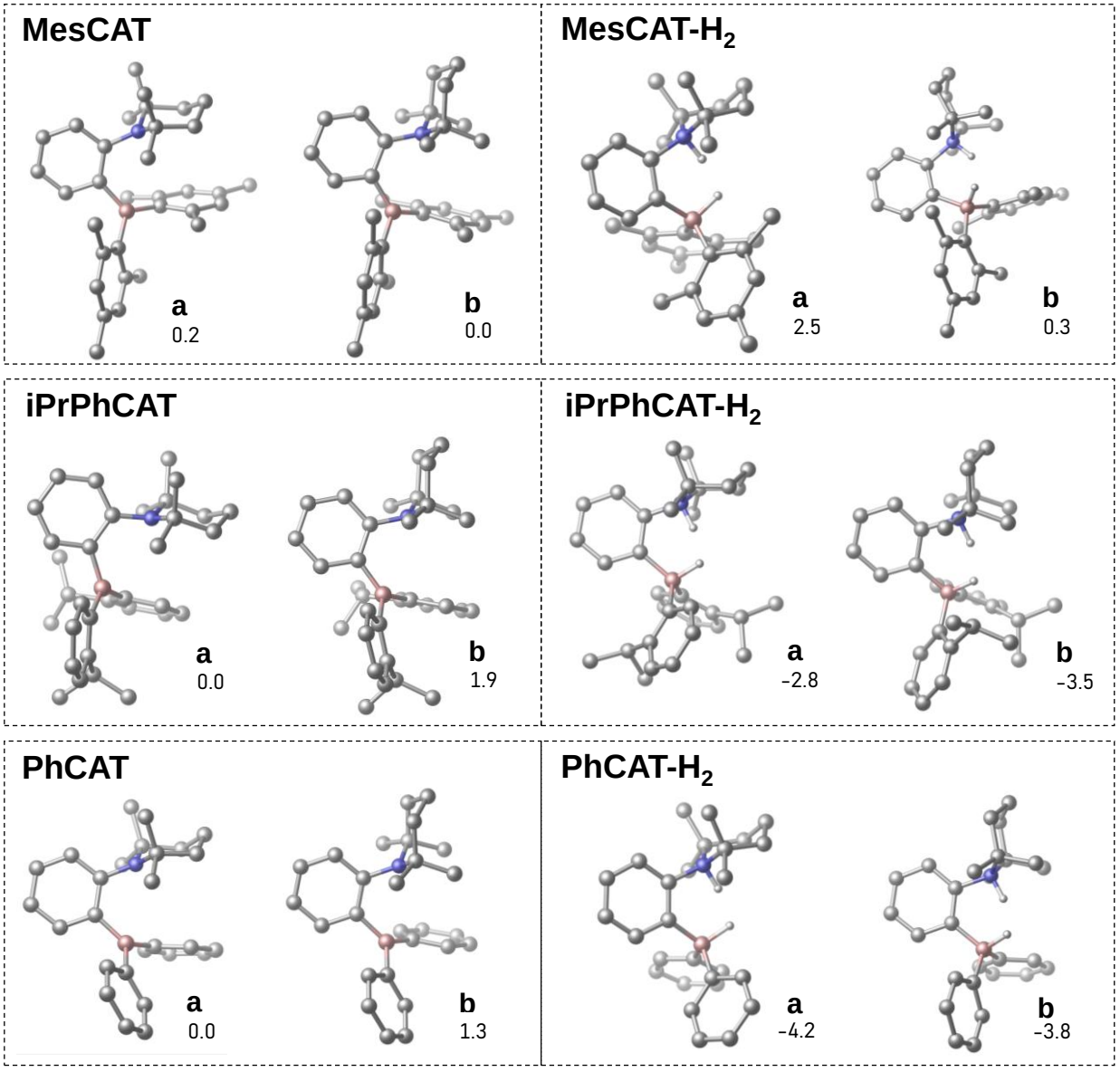

Figure S13. *Ansa*-aminoboranes and their H_2 adducts both in their **a** and their **b** conformers. Gibbs free energies in DCM are given in kcal/mol with respect to the most stable *ansa*-aminoborane conformer (and separated H_2).

Table S7. Relative stabilities of **a** and **b** TMP forms of the studied *ansa*-aminoboranes. Gibbs free energies in DCM are presented in kcal/mol with respect to the more stable conformer in all cases.

	Gibbs free energy of the conformer, kcal/mol	
Compound	**a**	**b**
PhCAT	0.0	1.3
MesCAT	0.2	0.0
iPrPhCAT	0.0	1.9
PhCAT-H_2	0.0	0.4
MesCAT-H_2	1.6	0.0
iPrPhCAT-H_2	5.4	0.0

It is apparent that the **a**-form is slightly more stable for the studied *ansa*-aminoboranes except for **MesCAT**, which is sterically the most hindered. Indeed, in the **a**-form of **MesCAT**, the aromatic ring of the mesityl group is slightly distorted due to steric repulsion between the methyl groups of the mesityl and the TMP unit. In the H_2 adducts, the **b**-form is generally favored. We demonstrated for **PhCAT** that transformation between the **a**- and **b**-forms may proceed rapidly at room temperature in several steps (the largest barrier is 14.0 kcal/mol in the investigated mechanism). The transition structures and the intermediates of the rearrangement are depicted in Figure S14.

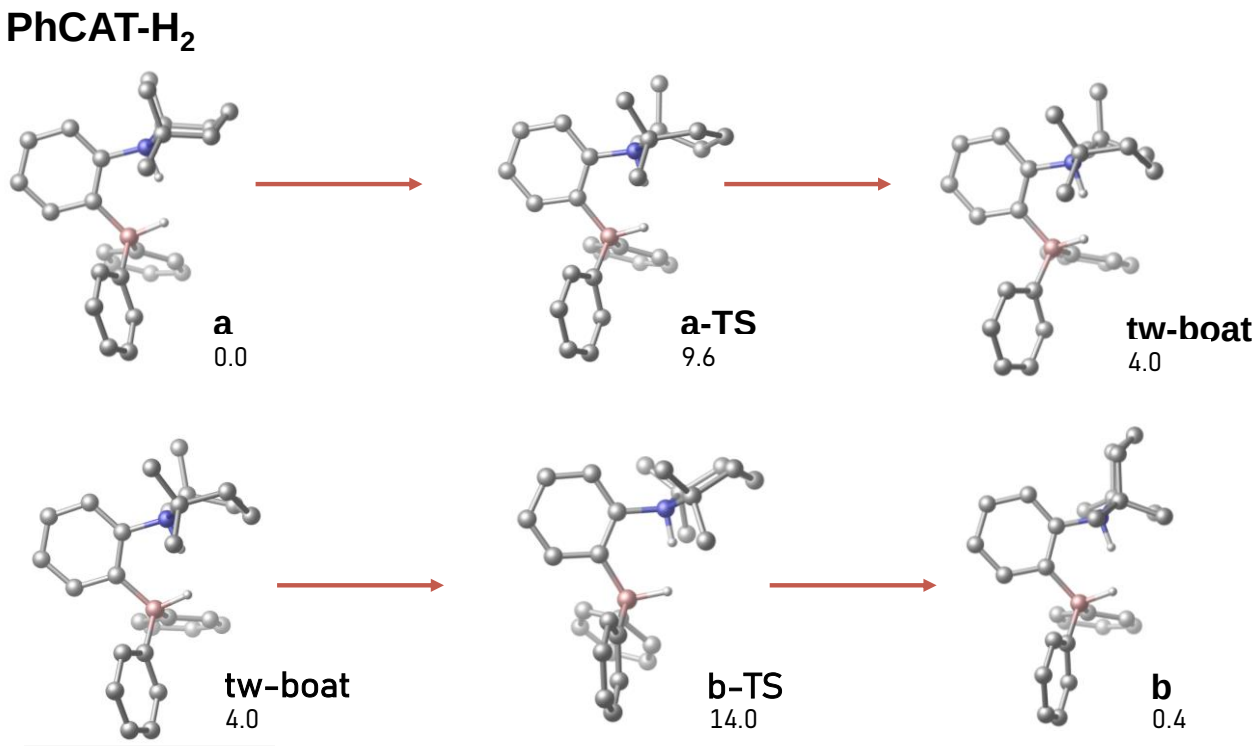

Figure S14. A plausible mechanism for the rearrangement of the TMP unit from **a** to **b** in the **PhCAT-H2**. Gibbs free energies in DCM are given in kcal/mol with respect to the **a**-form of **PhCAT-H2**.

2.2 Thermodynamics and kinetics of the H_2 activation

The stability data of the H_2 adducts in different solvents are presented in Table S8. We found that the formation of the adduct is more favored in polar solvents and particularly when the *ansa*-aminoborane is sterically less crowded. According to the calculations, with **PhCAT** and **iPrPhCAT**, the H_2 activation is possible even in toluene, whereas with **MesCAT**, the formation of the adduct is favored in highly polar solvents.

Table S8. Stabilities of the H_2 adducts in various solvents. Gibbs free energies of the most favored conformer of the adducts are given in kcal/mol with respect to the most favored conformer of the corresponding AAB and separated H_2.

	Gibbs free energy, kcal/mol			
Compound	Tol	DCM	MeCN	DMSO
PhCAT-H$_2$	-0.4	-4.2	-5.7	-5.9
MesCAT-H$_2$	3.1	0.3	-0.8	-1.2
iPrPhCAT-H$_2$	-0.2	-3.5	-4.2	-4.7

We investigated the mechanism of the H_2 activation with all the three *ansa*-aminoboranes starting from the **a**- and **b**- forms. In the case of **PhCAT** and **iPrPhCAT**, we found that the barrier of the hydrogen cleavage is lower in the **a**-conformer. The transition structures are depicted in Figure S15. With **MesCAT**, the formation of the H_2 adduct has a lower barrier in the **b**-form, and in this case the addition proceeds in two steps. The structures of the **a**- and **b**-forms of **MesCAT** are depicted in Figure S16. First, the hydrogen coordinates to the boron and is then cleaved to form the other bond with the nitrogen. The intermediate between the two transition states lies high and has no mechanistic importance.

The activation Gibbs free energies of the H_2 activation are summarized in Table S9. The barriers tend to be larger as the *ansa*-aminoborane becomes more crowded. Even though the H_2-adducts have different stabilities in various solvents, the solvent seems to have negligible effect on the barriers.

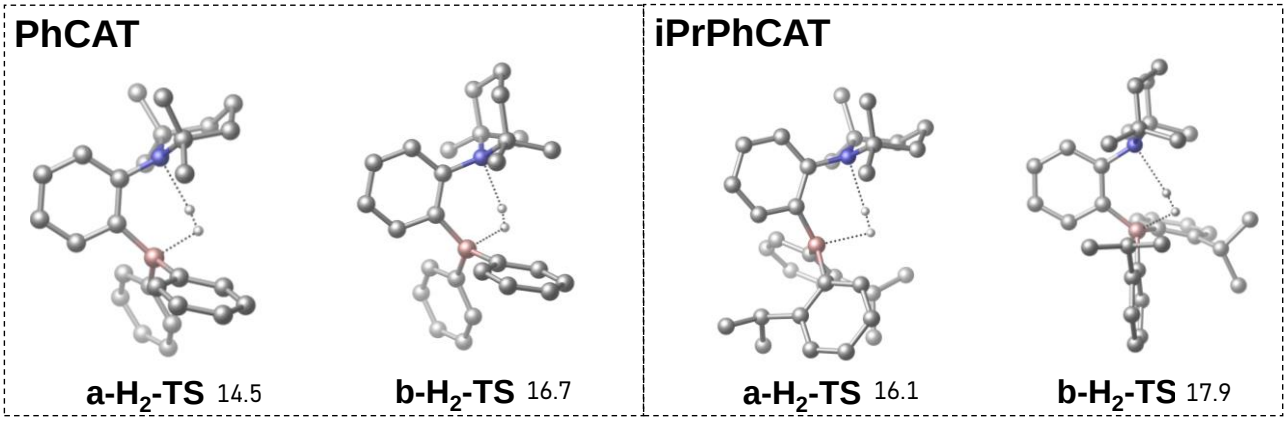

Figure S15. Structures of the transition states of the hydrogen cleavage with the *ansa*-aminoboranes **PhCAT** and **iPrPhCAT**. Gibbs free energies in DCM are given in kcal/mol with respect to separated **PhCAT** or **iPrPhCAT** in **a**-form and H_2.

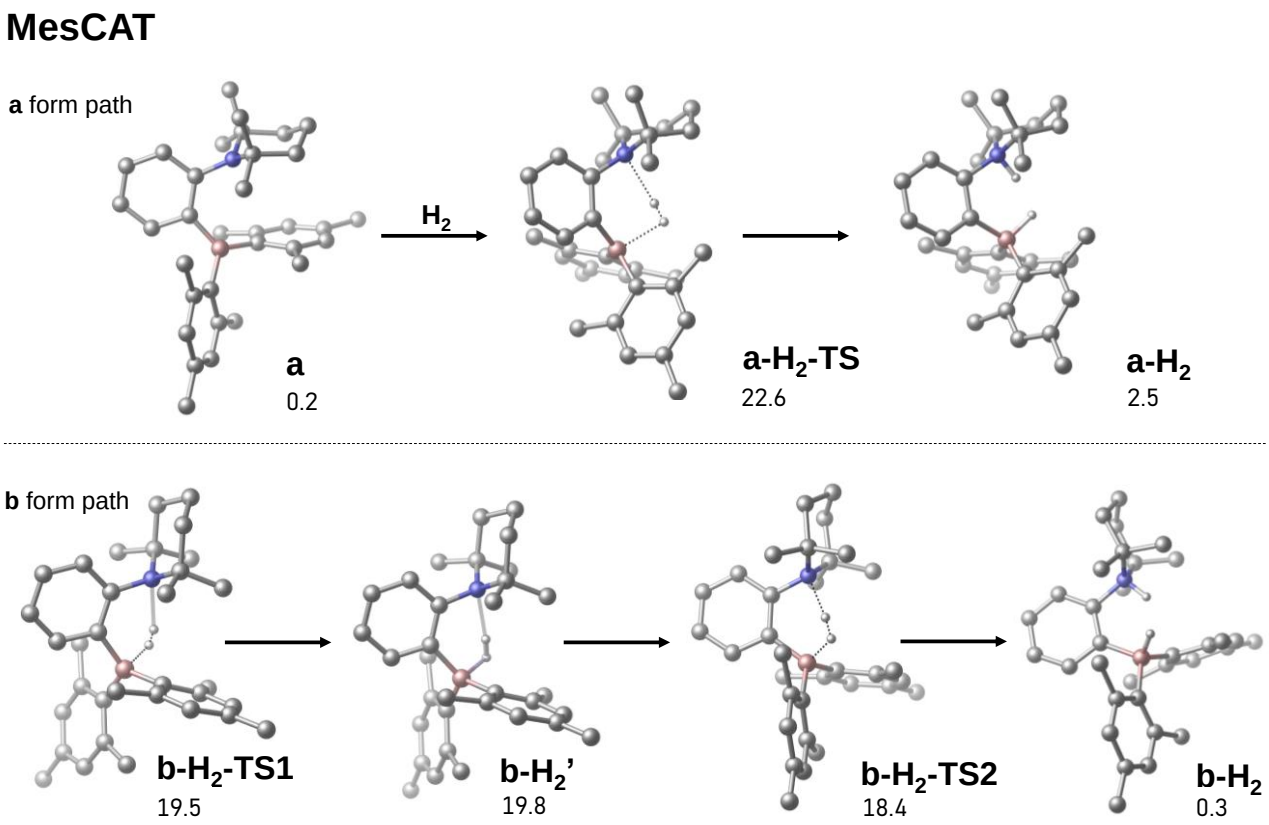

Figure S16. Mechanism of the H_2 activation with the **MesCAT** in **a-** (top) and **b**-forms (below). All Gibbs free energies in DCM are given in kcal/mol with respect to separated **MesCAT** in **b**-form and H_2.

Table S9. Barriers of the H_2 activation in various solvents. Activation Gibbs free energies corresponding to the most favored transition state are given with respect to the more favored *ansa*-aminoborane conformation and separated H_2 in kcal/mol.

	Gibbs free energy of H_2 activation, kcal/mol			
Compound	Tol	DCM	MeCN	DMSO
PhCAT	14.5	14.5	14.5	14.3
iPrPhCAT	16.2	16.1	16.6	16.2
MesCAT	19.4	19.5	19.4	19.2

2.3 Rotation of the borohydride site

It is crucial to know whether the *ansa*-aminoborane-H_2 adducts are present in several conformers. Apart from the possible rotation of the TMP unit between **a** and **b** forms, the rotation of the boryl unit may also be possible. In order to estimate the stability of further conformers and to find out whether the rotation is kinetically feasible, we carried out potential energy surface scans varying the C-C-B-H dihedral angle for all investigated *ansa*-aminoboranes. As an illustration, the varying dihedral is highlighted in Figure S17 for **PhCAT-H2**.

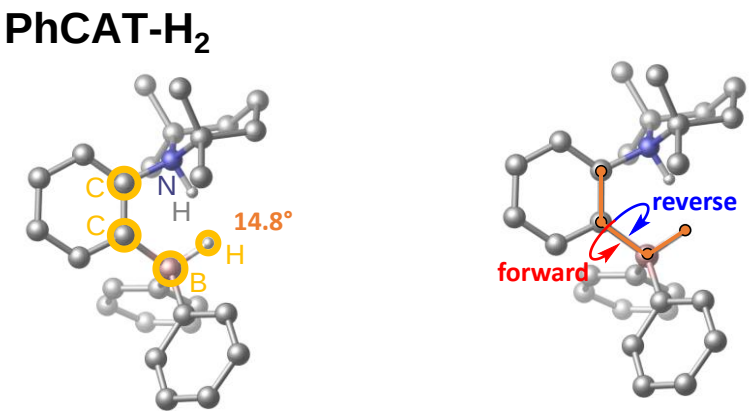

Figure S17. The rotation of the borohydride site of **PhCAT-H$_2$** in **a**-form. The dihedral angle between the highlighted C-C-B-H atoms (left) was changed systematically to find the rotated conformers both in the forward and the reverse directions (right).

The rotation of the borohydride site was investigated for AAB-H$_2$ species in the **a**-form as we demonstrated that rearrangement from the **a**- to **b**-form is a kinetically feasible process under ambient conditions (Figure S14). The following sections show the corresponding results for each AAB.

2.3.1 PhCAT-H$_2$

The rotamers of **PhCAT-H$_2$** and the transition states connecting them are depicted in Figure S18. The figure exemplifies **a**-form structure (see discussion in the section about TMP inversion). The conformer formed initially during the H$_2$-addition is the most stable one as the dihydrogen bonds between the B$^-$-H and the N$^+$H units are only present in this form. The conformers **Rot$_+$** and **Rot$_–$** have the same Gibbs free energies as they are enantiomers, and this is valid for the transition states **Rot$_+$-TS** and **Rot$_–$-TS** as well. The rotation between **Rot$_+$** and **Rot$_–$** is possible directly through the transition state **Rot$_±$-TS**. Both the barriers of the first and the second rotations are relatively low, so the rotation is clearly feasible at room temperature. However, the rotated form of **PhCAT-H$_2$** is 5.2 kcal/mol less stable than the original conformer, so it will only be present in a negligible ratio.

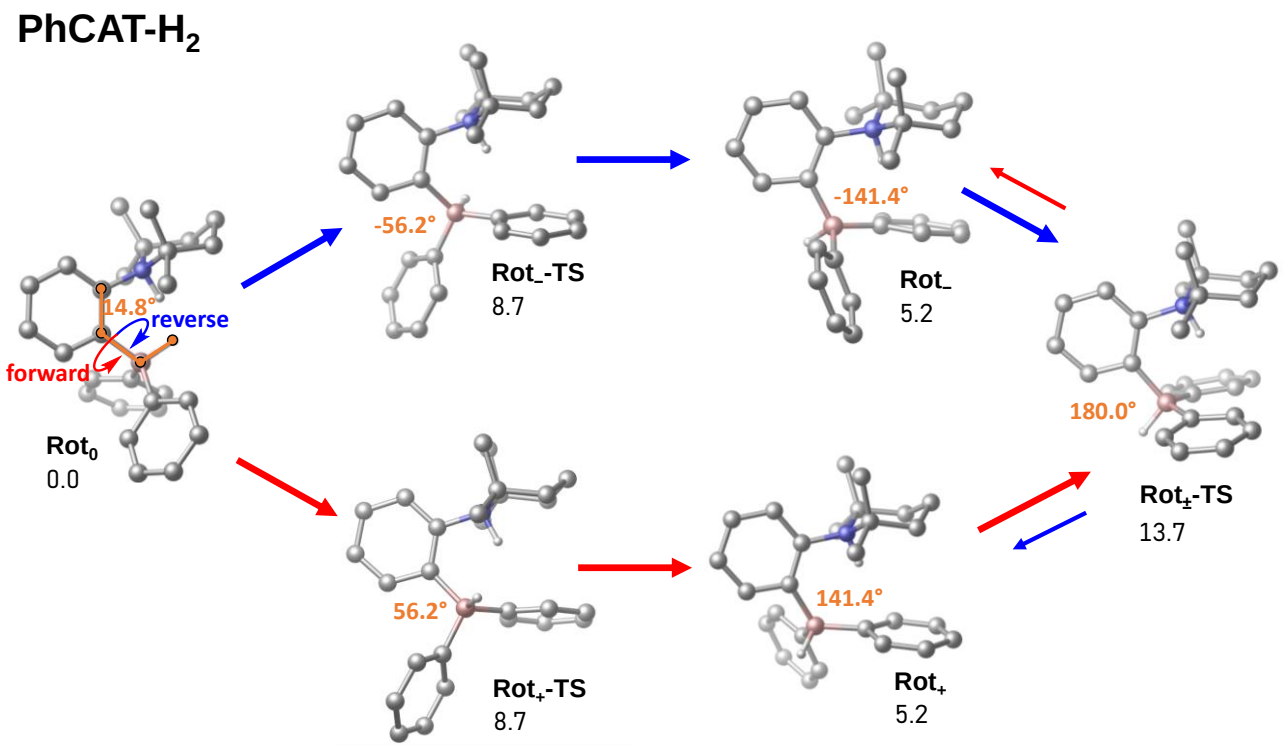

Figure S18. The rotation of the borohydride site of **PhCAT-H$_2$** in **a**-form. Gibbs free energies in DCM are given in kcal/mol with respect to the most stable **Rot$_0$** rotamer of **PhCAT-H$_2$**. Numbers in orange give the dihedral angles defined in figure S17.

2.3.2 iPrPhCAT-H$_2$

The rotamers of the **iPrPhCAT-H$_2$** and the related transition states are depicted in Figure S19. The figure exemplifies **a**-form structure (see discussion in the section about TMP inversion). **Rot$_+$** and **Rot$_-$** rotamers in this case have significantly different stabilities since the position of the isopropyl groups are different and these groups may be responsible for large steric strain. This difference is reflected in the transition states **Rot$_+$-TS** and **Rot$_-$-TS** as well. The transition state connecting the two rotated forms has even higher activation Gibbs free energy (18.5 kcal/mol), though this barrier is lower than in the analogous rotation of the **MesCAT-H$_2$** (25.8 kcal/mol, see below) and can be accessed at room temperature.

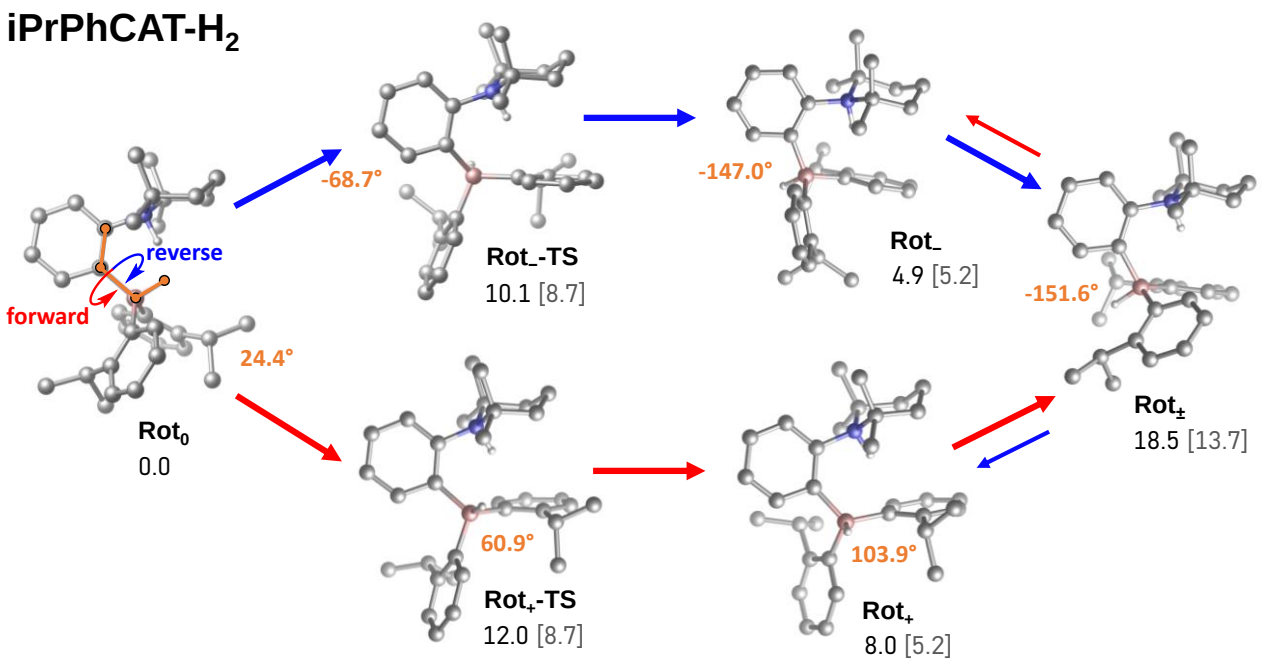

Figure S19. The rotation of the boryl site in **iPrPhCAT-H2**. Gibbs free energies in DCM are given in kcal/mol with respect to the most stable **Rot0** rotamer of **iPrPhCAT-H2**. Numbers in orange give the dihedral angles defined in figure S17.

The conclusion regarding the possible rotation of the borohydride site in **iPrPhCAT-H2** is the same as it was with the other two *ansa*-aminoboranes: the rotation is feasible, but since the rotated forms have relatively low stability, they are not expected to be present in a significant amount.

2.3.3 MesCAT-H2

The rotamers of **MesCAT-H2** and the corresponding transition structures are depicted in Figure S20. The figure exemplifies **a**-form structure (see discussion in the section about TMP inversion). **Rot+** and **Rot–** have the similar relative stabilities to the analogous rotamers of **PhCAT-H2** have with respect to the most stable **Rot0** rotamer of **PhCAT-H2**. In this case, however, the two conformers have slightly different Gibbs free energies as the orientation of the mesityl groups is not exactly the same in the two structures. The steric strain has a much larger effect in the transition states as the barriers are significantly higher than the analogous barriers with the **PhCAT-H2**. The direct rotation between the **Rot+** and the **Rot–** is not even feasible at room temperature (the corresponding barrier is 25.8 kcal/mol). In **Rot±-TS**, the rings of the mesityl groups are distorted from their optimal planar arrangement to reduce the steric repulsion between its methyl groups and the TMP unit. This distortion, however, also leads to a large increase in energy. In principle, both conformers can be reached from the original **Rot0** form of **MesCAT-H2** through an activation Gibbs free energy

approximately 15 kcal/mol, but since their relative stability is 5-6 kcal/mol, they will only be present in a low amount.

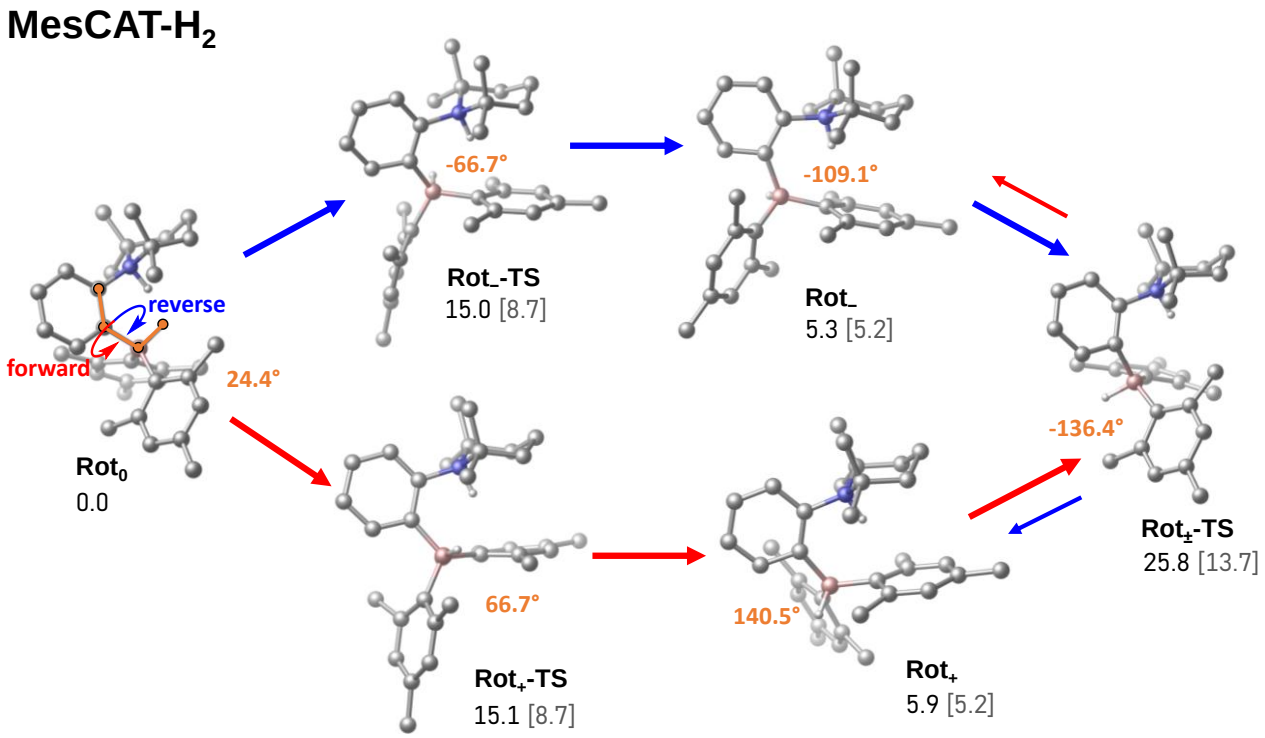

Figure S20. The rotation of the boryl site in **MesCAT-H2** in **a**-form. Gibbs free energies in DCM are given in kcal/mol with respect to the most stable **Rot0** rotamer of **MesCAT-H2**. Numbers in orange give the dihedral angles defined in figure S17.

3 References

S1. K. Sorochkina, V. V. Zhivonitko, K. Chernichenko, V. V. Telkki, T. Repo and I. V. Koptyug, *J. Phys. Chem. Lett.*, 2018, **9**, 903-907.

S2. V. V. Zhivonitko, K. Sorochkina, K. Chernichenko, B. Kotai, T. Foldes, I. Pápai, V.-V. Telkki, T. Repo and I. Koptyug, *Phys. Chem. Chem. Phys.*, 2016, **18**, 27784-27795.

S3. C. R. Bowers, in *Encyclopedia of Nuclear Magnetic Resonance*, eds. D. M. Grant and R. K. Harris, Wiley, Chichester, 2002, vol. 9, ch. Chapter, pp. 750-769.

S4. J. Keeler, *Understanding NMR spectroscopy*, Wiley, Oxford, 2nd ed. edn., 2010.

S5. M. B. Krüger, C. Selle, D. Heller and W. Baumann, *J. Chem. Eng. Data*, 2012, **57**, 1737-1744.

S6. E. Brunner, *J. Chem. Eng. Data*, 1985, **30**, 269-273.

S7. M. J. Frisch, G. W. Trucks, H. B. Schlegel, G. E. Scuseria, M. A. Robb, J. R. Cheeseman, G. Scalmani, V. Barone, G. A. Petersson, H. Nakatsuji, X. Li, M. Caricato, A. V. Marenich, J. Bloino, B. G. Janesko, R. Gomperts, B. Mennucci, H. P. Hratchian, J. V. Ortiz, A. F. Izmaylov, J. L. Sonnenberg, Williams, F. Ding, F. Lipparini, F. Egidi, J. Goings, B. Peng, A. Petrone, T. Henderson, D. Ranasinghe, V. G. Zakrzewski, J. Gao, N. Rega, G. Zheng, W. Liang, M. Hada, M. Ehara, K. Toyota, R. Fukuda, J. Hasegawa, M. Ishida, T. Nakajima, Y. Honda, O. Kitao, H. Nakai, T. Vreven, K. Throssell, J. A. Montgomery Jr., J. E. Peralta, F. Ogliaro, M. J. Bearpark, J. J. Heyd, E. N. Brothers, K. N. Kudin, V. N. Staroverov, T. A. Keith, R. Kobayashi, J. Normand, K. Raghavachari, A. P. Rendell, J. C. Burant, S. S. Iyengar, J. Tomasi, M. Cossi, J. M. Millam, M. Klene, C. Adamo, R. Cammi, J. W.

Ochterski, R. L. Martin, K. Morokuma, O. Farkas, J. B. Foresman and D. J. Fox, *Gaussian 16 Rev. E.01*, Wallingford CT, 2016.
S8. J. D. Chai and M. Head-Gordon, *Phys. Chem. Chem. Phys.*, 2008, **10**, 6615-6620.
S9. S. Grimme, *Chem. Eur. J.*, 2012, **18**, 9955-9964.
S10. A. V. Marenich, C. J. Cramer and D. G. Truhlar, *J. Phys. Chem. B*, 2009, **113**, 6378-6396.
S11. *Maestro, version 11.8. Schrödinger*, LLC, New York, https://www.schrodinger.com/maestro.
S12. K. Roos, C. J. Wu, W. Damm, M. Reboul, J. M. Stevenson, C. Lu, M. K. Dahlgren, S. Mondal, W. Chen, L. L. Wang, R. Abel, R. A. Friesner and E. D. Harder, *J. Chem. Theory Comput.*, 2019, **15**, 1863-1874.